



# Single-crystal elasticity of the deep-mantle magnesite at high pressure and temperature



Jing Yang <sup>a,\*</sup>, Zhu Mao <sup>a,b</sup>, Jung-Fu Lin <sup>a</sup>, Vitali B. Prakapenka <sup>c</sup>

<sup>a</sup> Department of Geological Sciences, Jackson School of Geosciences, The University of Texas at Austin, Austin, TX 78712, USA

<sup>b</sup> Laboratory of Seismology and Physics of Earth's Interior, School of Earth and Planetary Sciences, University of Science and Technology of China, Hefei, Anhui 230026, China

<sup>c</sup> GeoSoilEnviroCARS, The University of Chicago, Chicago, IL 60637, USA

## ARTICLE INFO

### Article history:

Received 13 August 2013

Received in revised form 12 December 2013

Accepted 15 January 2014

Available online xxxx

Editor: L. Stixrude

### Keywords:

single-crystal elasticity

magnesite

high pressure-temperature

Brillouin scattering

deep carbon

## ABSTRACT

Magnesite ( $\text{MgCO}_3$ ) is considered to be a major candidate carbon host in the Earth's mantle, and has been found to exist as an accessory mineral in carbonated peridotite and eclogite. Studying the thermal elastic properties of magnesite under relevant pressure-temperature conditions of the upper mantle is thus important for our understanding of the deep-carbon storage in the Earth's interior. Here we have measured the single-crystal elasticity of a natural magnesite using *in situ* Brillouin spectroscopy and X-ray diffraction in a diamond anvil cell up to 14 GPa at room temperature and up to 750 K at ambient pressure, respectively. Using the third-order Eulerian finite-strain equations to model the elasticity data, we have derived the aggregate adiabatic bulk,  $K_{50}$ , and shear moduli,  $G_0$ , at ambient conditions:  $K_{50} = 114.7 (\pm 1.3)$  GPa and  $G_0 = 69.9 (\pm 0.6)$  GPa. The pressure derivatives of the bulk and shear moduli at 300 K are  $(\partial K_S / \partial P)_T = 4.82 (\pm 0.10)$  and  $(\partial G / \partial P)_T = 1.75 (\pm 0.10)$ , respectively, while their temperature derivatives at ambient pressure are  $(\partial K_S / \partial T)_P = -24.0 (\pm 0.2)$  MPa/K and  $(\partial G / \partial T)_P = -14.8 (\pm 0.7)$  MPa/K. Based on the thermal elastic modeling of the measured elastic constants along an expected normal upper-mantle geotherm and a cold subducting slab, magnesite exhibits compressional wave ( $V_P$ ) anisotropy of approximately 46–49% and shear wave ( $V_S$ ) splitting of 37–41% that are much larger than those of major constituent minerals in the Earth's upper mantle including olivine, pyroxene, and garnet. The modeled aggregate  $V_P$  and  $V_S$  velocity in moderately carbonated peridotite and eclogite containing approximately 10 wt.% magnesite (approximately 5 wt.%  $\text{CO}_2$ ) show minimal effects of magnesite on the seismic profiles of these rock assemblages at upper mantle conditions, suggesting that the presence of magnesite is likely difficult to be detected seismically. However, due to its unusually high  $V_P$  and  $V_S$  anisotropies, magnesite with strong preferred orientations may exhibit sufficient  $V_P$  and  $V_S$  anisotropies that can have significant influences on seismic anisotropies of the regionally carbonated upper mantle.

© 2014 Elsevier B.V. All rights reserved.

## 1. Introduction

Carbon transport and storage in the deep Earth interior have attracted in recent years the attention of researches because of a growing recognition of their key importance for the global carbon cycle and their influence on (e.g. Burton et al., 2013). Two processes of particular relevance are the transport of carbon into the Earth interior (ingassing) through slab subductions and the outgassing of carbon via magmatic and volcanic processes (e.g. Hazen et al., 2012). Based on the geochemical and petrological estimates on the carbon contents of the mantle-derived car-

bonated samples, the total carbon budget in the planet's mantle can be in the order of  $(0.8\text{--}12.5) \times 10^{23}$  g of C, whereas the amount of carbon in the near-surface reservoirs, including the crust, oceans, and atmosphere is in the order of  $(8.4\text{--}10.2) \times 10^{22}$  g of C (Hirschmann and Dasgupta, 2009; Dasgupta and Hirschmann, 2010). Therefore, Earth's mantle is likely the largest carbon reservoir of the planet, in which the mass of the deep-mantle carbon can well exceed that in all other carbon reservoirs. As a result of the variable pressure-temperature ( $P$ - $T$ ) and oxygen fugacity conditions in the Earth's interior, deep-mantle carbon can exist in a number of forms including  $\text{CO}_2$ -rich and hydrocarbon-rich fluids/melts, accessory minerals (carbonates, diamond, and graphite), iron carbides, among others (Dasgupta and Hirschmann, 2010; Kaminsky and Wirth, 2011). A new recent study reports that

\* Corresponding author.

carbon also can be stored in oxides crystal defects at mantle conditions (Wu and Buseck, 2013).

Carbonates are likely the stable crystalline accessory carbon-bearing phases in the subducted carbonated oceanic crusts of the transition zone (Luth, 1999). Calcite and dolomite carbonates ( $\text{CaCO}_3$  and  $(\text{Ca},\text{Mg})\text{CO}_3$ ), however, are stable only at  $P$ - $T$  conditions at shallower parts of the upper mantle, e.g., at depth above ~120 km (~4 GPa); though, recent studies have suggested that these minerals can remain stable at higher  $P$ - $T$  conditions within the Earth (Oganov et al., 2006; Mao et al., 2011). On the other hand, recent experimental and theoretical studies on the phase diagram of magnesite have shown that magnesite remains stable in the  $\text{MgCO}_3$  form at expected  $P$ - $T$  conditions of the lower mantle, whereas new high-pressure phases of magnesite have been reported to occur at lowermost-mantle conditions (Ishikiri et al., 2004; Oganov et al., 2008; Boulard et al., 2011), making magnesite a potential major deep-carbon host in the deeper parts of the mantle. Furthermore, observations of carbonate inclusions in natural diamonds thought to be originated from the lower mantle further support the notion that magnesite can be a major deep-carbon host (Brenker et al., 2007). Most recent results also show that magnesite can be formed from reactions of  $\text{MgO}$  and  $\text{CO}_2$  at  $P$ - $T$  conditions of the Earth's mantle (Scott et al., 2013). Therefore, studying the physical and chemical properties of magnesite under relevant  $P$ - $T$  conditions of the mantle can hold the key to our understanding of the global carbon cycle as well as to identifying potential carbonate-rich regions in the deep Earth interior.

Of particular importance to seismic and geochemical modeling of the deep-Earth carbonates is the high  $P$ - $T$  elasticity of magnesite at relevant conditions of the Earth's mantle. Laboratory measurements on the sound velocities of magnesite and other carbonates at ambient conditions have been used to assess the seismic detectability of carbonated eclogite and peridotite in the upper mantle. These studies have suggested that moderately carbonated regions may be difficult to detect seismically (Sanchez-Valle et al., 2011). Nevertheless, high  $P$ - $T$  effects on the sound velocities of magnesite remain mostly unavailable; specifically, the pressure effect on the sound velocities of magnesite have been measured only up to 1 GPa (Christensen, 1972) and there are not yet published high-temperature data.

Here we have measured the compressional wave ( $V_P$ ) and shear wave ( $V_S$ ) velocities of single-crystal magnesite using Brillouin Light Scattering (BLS) Spectroscopy in a high-pressure diamond anvil cell (DAC) up to 13.7 GPa at 300 K and up to 750 K at ambient pressure, respectively. Based on the experimentally-measured velocities, we have derived the full elastic stiffness tensor and have modeled the elasticity and elastic anisotropies of magnesite at expected upper-mantle  $P$ - $T$  conditions. These results are applied to understand the potential effects of magnesite on the seismic profiles and anisotropies in carbonated eclogite and peridotite in the upper mantle. Our modeled velocity profiles provide mineral physics references and constraints for future seismic detections of potentially carbonated regions in the Earth's interior.

## 2. Experimental details

Natural single-crystal magnesite from Bahia, Brazil was obtained from the Vargas Mineral Collection at the Jackson School of Geosciences, the University of Texas at Austin (Collection number: V3782). Electron microprobe analyses of the starting sample revealed a homogeneous chemical composition of  $\text{MgCO}_3$  with less than 0.5 mol.% Mn and Fe in total, while X-ray diffraction (XRD) measurements showed that the sample had a rhombohedral structure (space group:  $R\bar{3}c$ ) with lattice parameters  $a = 4.6431 (\pm 0.0049)$  Å and  $c = 15.0353 (\pm 0.0074)$  Å, consistent with the lattice parameters of magnesite reported previ-

ously (Ross, 1997). The single-crystal sample was cleaved using a knife along the rhombohedral cleavages parallel to  $\{10\bar{1}\}$  planes. Cleaved platelets showing high optical clarity and surface smoothness were selected for BLS measurements. Some cleaved platelets when screened for BLS spectral quality and were found to contain polysynthetic twinning that showed up in BLS spectra with two  $V_P$  peaks at certain given orientations; these samples and their BLS spectra were eventually discarded.

High-pressure BLS measurements were conducted on single-crystal magnesite without the polysynthetic twinning in a DAC in the Mineral Physics Laboratory of the University of Texas at Austin. A single-crystal platelet with a diameter of 150 µm and thickness of 35 µm was loaded into the sample chamber of a short symmetrical DAC with a pair of diamond culets of 400 µm having Ne as the pressure medium and ruby spheres as the pressure calibrant (Mao et al., 1986). The sample chamber was made of a Re gasket with a pre-indented thickness of 70 µm and a drilled hole of 220 µm. The Brillouin system was equipped with a Coherent Verdi V2 laser with a wavelength of 532 nm, a Perkin-Elmer photomultiplier detector (PMT; model: MP983), and a JRS six-pass tandem Fabry-Pérot interferometer (Lu et al., 2013). The laser beam was focused down to approximately 20 µm in diameter at the sample position. The scattered Brillouin signals were collected with a scattering angle of 47.9° which was calibrated using the elastic constants of standard silicate glass, distilled water, and single-crystal  $\text{MgO}$  (Ostwald et al., 1977; Sinogeikin and Bass, 2000; Polian et al., 2002). Pressures were measured from the ruby sphere next to the sample, and pressure uncertainties ( $\pm 1\sigma$ ) were calculated using multiple measurements before and after the collection of the Brillouin spectra.

High-temperature BLS experiments were performed at 13BMD of the GSECARS Sector, Advanced Photon Source (APS), Argonne National Laboratory (ANL) (Sinogeikin et al., 2006). A single-crystal magnesite sample was loaded into an externally-heated DAC (EHDAC) having Pt wires as the external resistive heating element and a Re gasket sample chamber (Kantor et al., 2012; Mao et al., 2012). The sample was sealed in a pre-indented and drilled hole of the sample chamber in the Re gasket to prevent any potential chemical reaction with air. An R-type thermocouple was attached to one of the diamond's surface approximately 500 µm away from its culet for temperature measurements; such experimental geometry permitted temperature uncertainties of within 1 K within our experiments (Sinogeikin et al., 2006). Single-crystal X-ray diffraction patterns of the magnesite were also collected using a CCD detector in order to determine the lattice parameters and hence density of the sample at high temperatures.

## 3. Results and data analyses

Brillouin spectra of magnesite were collected up to 14 GPa at room temperature in a 1–3 GPa pressure interval and up to 750 K at room pressure. The BLS spectra were collected in the  $\{10\bar{1}\}$  plane in approximately 19 to 37 different crystallographic directions (at approximately 5 to 10 degrees interval) for each given  $P$ - $T$  condition. Most of the spectra showed strong  $V_P$  and two polarized  $V_S$  peaks with high signal-to-noise ratios, although the  $V_P$  or  $V_S$  peaks were weaker in a number of directions as expected due to the intrinsic anisotropy of the elasto-optic coupling in trigonal magnesite (Nelson et al., 1972) (Fig. 1). Brillouin signals of the Ne pressure medium were also observed at pressures below 8 GPa, but they were not as visible at higher pressures. The measured  $V_P$  and  $V_S$  varied significantly as a function of the azimuthal angle, immediately indicating strong elastic anisotropies of the sample at high  $P$  and high  $T$  (Fig. 2).

Since the  $V_P$  and  $V_S$  are intrinsically a function of crystallographic direction and deriving the full elastic constants requires

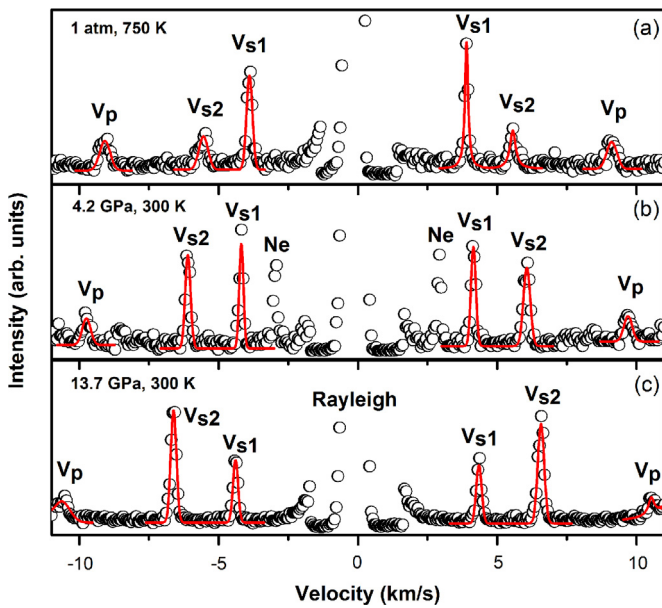


**Fig. 1.** Representative Brillouin spectra of single-crystal magnesite. (a) 1 atm, 750 K; (b) 4.2 GPa, 300 K; (c) 13.7 GPa, 300 K.

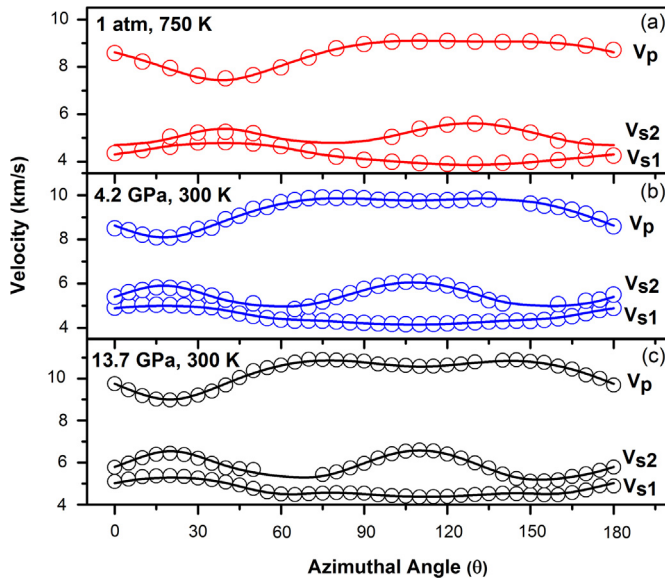


**Fig. 2.**  $V_p$  and  $V_s$  velocities of single-crystal magnesite as a function of the azimuthal angle measured from a cleaved  $\{1, 0, -1, 0\}$  platelet. (a) 1 atm, 750 K; (b) 4.2 GPa, 300 K; (c) 13.7 GPa, 300 K.

the knowledge of the sample's density, we have followed a nonlinear inversion procedure proposed previously to solve the six elastic constants of the rhombohedral magnesite using the Christoffel's equations with initial densities from an equation of state (EoS) of magnesite (Every, 1980; Chen et al., 2001; Litasov et al., 2008; Sanchez-Valle et al., 2011). Excellent agreement is found between the measured and calculated sound velocities from the best-fit elastic model at ambient and high  $P$ - $T$  conditions (Fig. 2). The derived single-crystal elastic constants of magnesite at ambient conditions are consistent with previous results within experimental errors validating our nonlinear inversion model for deriving the elastic constants of magnesite at high  $P$  and high  $T$  (Tables S1 and S2). The root-mean-square deviation (RMS) for the fitting is about 50–55 m/s. The modeled sound velocities are in excellent agreement with the experimental results at high pressure and high temperatures.

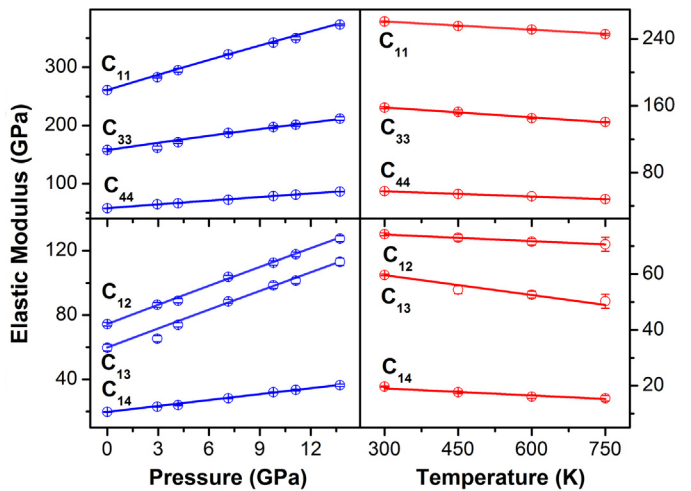


**Fig. 3.** Single-crystal elastic constants of magnesite at the experimental pressures and temperatures. Open circles: experimental results; blue lines: modeled results using the finite-strain fitting; red lines: modeled results using a linear fitting. (For interpretation of the references to color in this figure legend, the reader is referred to the web version of this article.)

Using the derived elastic constants of the sample, the aggregate adiabatic bulk and shear moduli ( $K_S$  and  $G$ ) were calculated using the Voigt–Reuss–Hill averages (Hill, 1952). The derived adiabatic bulk ( $K_{S0}$ ) and shear moduli ( $G_0$ ) are at ambient conditions are  $114.7 (\pm 1.3)$  and  $69.9 (\pm 0.6)$  GPa, respectively. An iterative procedure was adopted to further obtain the finite strain parameters for individual and aggregate elastic moduli as well as densities at high pressure. The pressure derivatives of the elastic moduli at 300 K were obtained by fitting the moduli at high pressure using the third-order Eulerian finite-strain equation of state (EoS) (Birch, 1978):

$$K_S = K_{S0}(1+2f)^{5/2}\{1 + [3((\partial K_S/\partial P)_T - 5)f]\},$$

$$G = (1+2f)^{5/2}[G_0 + (3K_{S0}(\partial G/\partial P)_T - 5G_0)f],$$

$$f = (1/2)[(V_0/V)^{2/3} - 1],$$

where  $(\partial K_S/\partial P)_T$  and  $(\partial G/\partial P)_T$  are the pressure derivative of the  $K_S$  and  $G$  at 300 K, respectively,  $f$  is the Eulerian strain, and  $V_0$  and  $V$  are unit-cell volume at ambient pressure and high pressure, respectively. The derived  $K_S$  and  $(\partial K_S/\partial P)_T$  were further converted to the isothermal bulk modulus ( $K_T$ ) and its pressure derivative at constant temperature  $(\partial K_T/\partial P)_T$  using the following thermodynamic relations (Poirier, 2000):

$$K_{T0} = K_{S0}/(1 + \alpha\gamma T),$$

$$(\partial K_T/\partial P)_T = (1 + \alpha\gamma T)^{-1}[(\partial K_S/\partial P)_T - \gamma T/K_{T0}(\partial K_T/\partial T)_P],$$

where  $(\partial K_T/\partial T)_P$  is the temperature derivative of the  $K_T$  at constant pressure,  $K_{T0}$  is the isothermal bulk modulus at ambient conditions,  $\alpha$  is the thermal expansion coefficient, and  $\gamma$  is the Grüneisen parameter. Literature values of  $(\partial K_T/\partial T)_P = -13 (\pm 1)$  (MPa/K),  $\alpha = a_0 + a_1 T$  with  $a_0 = 4.03 (\pm 0.07) \times 10^{-5}$  K $^{-1}$  and  $a_1 = 0.49 (\pm 0.10) \times 10^{-8}$  K $^{-2}$ , and  $\gamma = 1.38 (\pm 0.01)$  were used for the conversion (Litasov et al., 2008). The  $K_T$  and  $(\partial K_T/\partial P)_T$  were used to construct the isothermal EoS and refined densities. We note that the parameters used in the formula including  $(\partial K_T/\partial T)_P$ ,  $\alpha$ , and  $\gamma$  were approximately derived from literature values. The aforementioned procedures were iterated numerically until both  $K_T$  and  $(\partial K_T/\partial P)_T$  values were self-consistent with the input densities (Litasov et al., 2008).

Using the modeled thermal EoS values and the third-order Eulerian finite-strain equations (Birch, 1978), the pressure derivatives

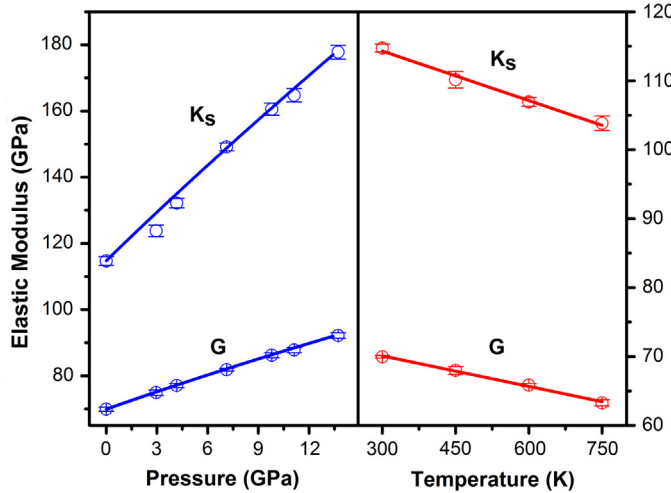


**Fig. 4.** Adiabatic bulk and shear modulus of magnesite at the experimental pressures and temperatures. Open circles: experimental results; solid lines: modeled fitting. A third-order Birch–Murnaghan equation of state was applied to model the high-pressure data, while the high-temperature data were linearly fitted.

**Table 1**  
Pressure and temperature derivatives of elastic moduli.

Pressure derivatives		Temperature derivatives (MPa/K)	
$(\partial C_{11}/\partial P)_T$	8.64 ( $\pm 0.07$ )	$(\partial C_{11}/\partial T)_P$	-33.0 ( $\pm 1.4$ )
$(\partial C_{33}/\partial P)_T$	4.20 ( $\pm 0.02$ )	$(\partial C_{33}/\partial T)_P$	-39.6 ( $\pm 3.0$ )
$(\partial C_{44}/\partial P)_T$	2.16 ( $\pm 0.02$ )	$(\partial C_{44}/\partial T)_P$	-20.9 ( $\pm 0.6$ )
$(\partial C_{12}/\partial P)_T$	3.91 ( $\pm 0.06$ )	$(\partial C_{12}/\partial T)_P$	-7.9 ( $\pm 0.6$ )
$(\partial C_{13}/\partial P)_T$	3.80 ( $\pm 0.01$ )	$(\partial C_{13}/\partial T)_P$	-23.7 ( $\pm 3.0$ )
$(\partial C_{14}/\partial P)_T$	1.21 ( $\pm 0.02$ )	$(\partial C_{14}/\partial T)_P$	-8.4 ( $\pm 0.2$ )
$(\partial K_S/\partial P)_T$	4.82 ( $\pm 0.10$ )	$(\partial K_S/\partial T)_P$	-24.0 ( $\pm 0.2$ )
$(\partial G/\partial P)_T$	1.75 ( $\pm 0.01$ )	$(\partial G/\partial T)_P$	-14.8 ( $\pm 0.7$ )

of the  $K_S$  and  $G$  were derived to be  $(\partial K_S/\partial P)_T = 4.82 (\pm 0.10)$ , and  $(\partial G/\partial P)_T = 1.75 (\pm 0.01)$  (Figs. 3 and 4, Table S3). Due to the limited temperature range for the high-temperature data, a linear equation was applied to obtain the temperature derivatives of the elastic moduli (Figs. 3 and 4, Table S3). The temperature derivative of the elastic moduli are:  $(\partial K_S/\partial T)_P = -24.0 (\pm 0.2)$  (MPa/K), and  $(\partial G/\partial T)_P = -14.8 (\pm 0.7)$  (MPa/K). The pressure and temperature derivatives of the six individual elastic constants are listed in Table 1. We have further analyzed our elasticity data using a more complete version of third-order Eulerian strain equation derived from Helmholtz free energy in Eulerian finite strain that has been reported in Stixrude and Lithgow-Bertelloni (2005). The results between the two methods, Birch (1978) and Stixrude and Lithgow-Bertelloni (2005) are consistent with each other within uncertainties (see Table S4 for details). The aggregate  $V_P$  and  $V_S$  velocities at high  $P$ – $T$  conditions (Fig. 5) were also calculated using:

$$V_P = \sqrt{\frac{K_S + \frac{4}{3}G}{\rho}}, \quad V_S = \sqrt{\frac{G}{\rho}}.$$

The measured elastic constants of magnesite at high  $P$ – $T$  permit us to evaluate its azimuthal velocity anisotropy which describes the velocity as a function of the wave propagation direction (Fig. 6). The  $V_P$  and  $V_S$  velocities propagation normal and parallel to the rotation axis show that  $V_P$  travels fastest along the  $[2, \bar{1}, \bar{1}, 0]$  direction and slowest along the rotation  $c$ -axis, indicating that the  $c$ -axis is the most compliant orientation. Furthermore, the  $V_{S1}$  is slowest along the  $[2, \bar{1}, \bar{1}, 0]$  direction and fastest along the  $c$ -axis, while  $V_{S2}$  propagates fastest along the  $[0, \bar{1}, 1, 0]$  and

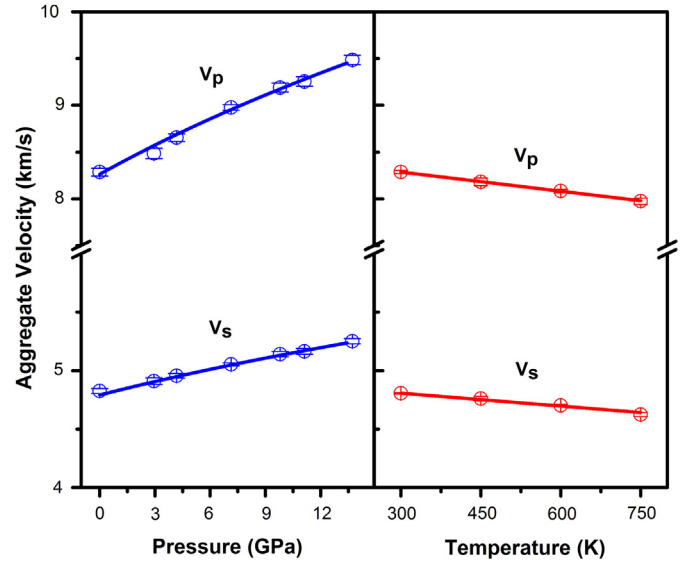


**Fig. 5.** Aggregate compressional and shear velocity of magnesite at representative pressure and temperature. Open circles: experimental data; solid lines: modeled results. A third-order Birch–Murnaghan equation of state was applied to model the high-pressure data, while the high-temperature data were linearly fitted.

slowest along the  $[2, \bar{1}, \bar{1}, 0]$  direction. These results immediately show extremely strong  $V_P$  and  $V_S$  anisotropies of magnesite. The azimuthal  $V_P$  and  $V_S$  anisotropies can also be analyzed using the anisotropy factor (Mainprice et al., 2000). The anisotropy factor for  $V_P$  ( $A_P$ ) is defined as:

$$A_P = 2 \times (V_{P,\max} - V_{P,\min}) / (V_{P,\max} + V_{P,\min}) \times 100\%,$$

where  $V_{P,\max}$  and  $V_{P,\min}$  represent the maximum and minimum  $V_P$  velocities of the mineral, respectively. The polarization anisotropy factor for  $V_S$  ( $A_S$ ; also called as the shear-wave splitting factor) is the percentage difference in the velocity of the two shear waves propagation in a given direction, and is defined as:

$$A_S = (V_{S1} - V_{S2}) / V_S \times 100\%,$$

where  $V_{S1}$  and  $V_{S2}$  are two orthogonally polarized  $V_S$  velocities, and  $V_S$  represents aggregate  $V_S$  velocity. Our results show that magnesite exhibits the azimuthal  $V_P$  anisotropy of 26.2% and the shear wave splitting anisotropy of 36.2% at ambient conditions, consistent with previous results (Hubert and Plicque, 1972; Heard, 1984; Chen et al., 2006; Sanchez-Valle et al., 2011) (Table S2). At elevated high  $P$ – $T$  conditions, these anisotropies increase with increasing  $P$ – $T$ ; the anisotropies increases by 4–5% at 13.7 GPa and approximately 2% at 750 K (Table S1 and Fig. 7).

#### 4. Modeling of velocity and anisotropy profiles for the upper mantle minerals

Here we report the first high pressure and temperature derivatives of elastic moduli of single-crystal magnesite by BLS experiments, and have applied the high  $P$ – $T$  elasticity results to understand the potential effects of magnesite on the seismic velocities and anisotropies of carbonated eclogite and peridotite. Carbonated eclogite is believed to carry significant amount of carbon into the deep upper mantle in which magnesite may exist as an accessory mineral through subduction-related dehydration or partial melting processes (Yaxley and Green, 1994; Molina and Poli, 2000). In addition, magnesite has been found to be likely the only stable carbonate in the most abundant upper-mantle rock assemblage, peridotite, at above 3.5 GPa (e.g. Brey et al., 1983, 2008).

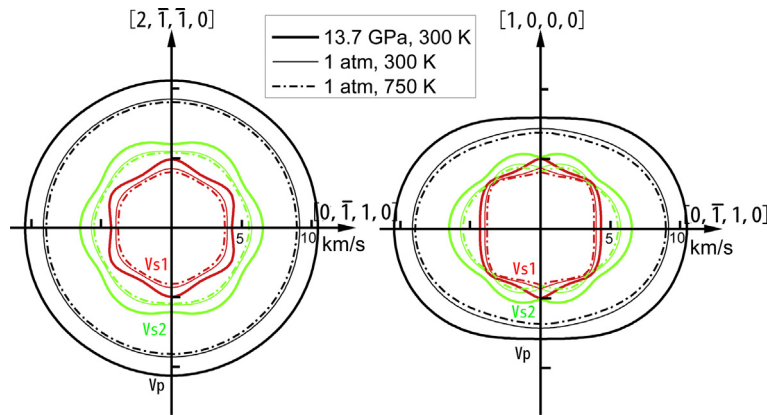


**Fig. 6.** Velocity of the compressional and shear wave propagation in a single-crystal magnesite. (a) Propagation normal to the rotation axis; (b) parallel to rotation axis. Red, green and black lines represent  $V_{S1}$ ,  $V_{S2}$  and  $V_p$ , respectively. (For interpretation of the references to color in this figure legend, the reader is referred to the web version of this article.)

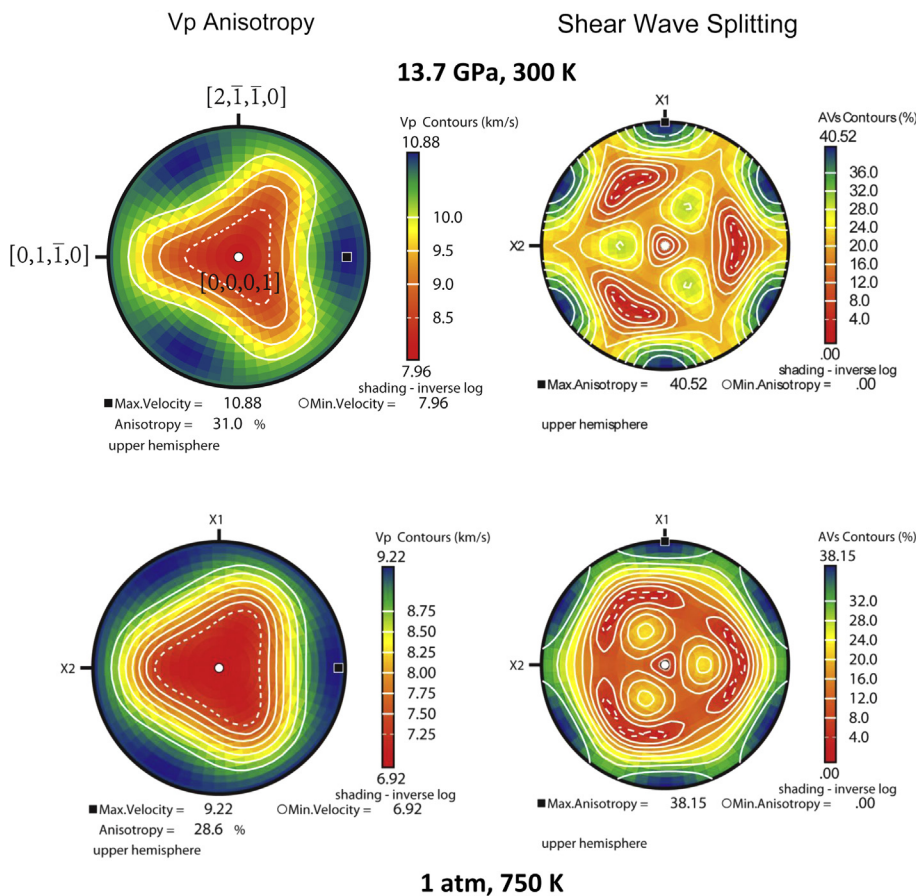


**Fig. 7.** Azimuthal  $V_p$  anisotropy and shear wave splitting of single-crystal magnesite at representative pressure and temperature.  $X_1$ ,  $X_2$  represent the crystallographic direction of  $[2, \bar{1}, \bar{1}, 0]$  and  $[0, 1, \bar{1}, 0]$  for hexagonal indexing. Calculations are performed using the petrophysical software Unicef Careware of D. Mainprice (1990).

#### 4.1. Sound velocities of magnesite at relevant $P-T$ conditions of the upper mantle

Based on our high  $P-T$  elasticity results for single-crystal magnesite, we have calculated the aggregate  $V_p$  and  $V_S$  profiles of magnesite using the Voigt-Reuss-Hill averages along an expected geotherm for cold subducted slabs and for the normal upper mantle, respectively (Dziewonski and Anderson, 1981; Brown and Shankland, 1981; Peacock, 2003) (Fig. 8). For direct comparison, seismic profiles of major minerals in upper-mantle eclogite and peridotite rock assemblages were calculated including olivine (Isaak, 1992; Zha et al., 1998; Liu and Li, 2006), clinopyroxene

(Cameron, 1973; Finger and Ohashi, 1976; Duffy and Anderson, 1989; Collins and Brown, 1998), orthopyroxene (Chai et al., 1997; Jackson et al., 2003, 2007), and garnet (Thieblot et al., 1998; Lu et al., 2013) (Fig. 8). Literature values for  $K_S$ ,  $G$ , and the thermal expansion coefficients were used for the calculations. Briefly, these values were further evaluated along a normally expected upper-mantle geotherm (Dziewonski and Anderson, 1981; Brown and Shankland, 1981) and a cold slab geotherm (Peacock, 2003) by extrapolating the experimentally-derived elastic moduli and their  $P-T$  derivatives to relevant  $P-T$  conditions using the third-order Eulerian finite-strain and Birch-Murnaghan EoS (Birch, 1978). Our modeled  $P-T$  conditions focus on the upper-mantle region ranging

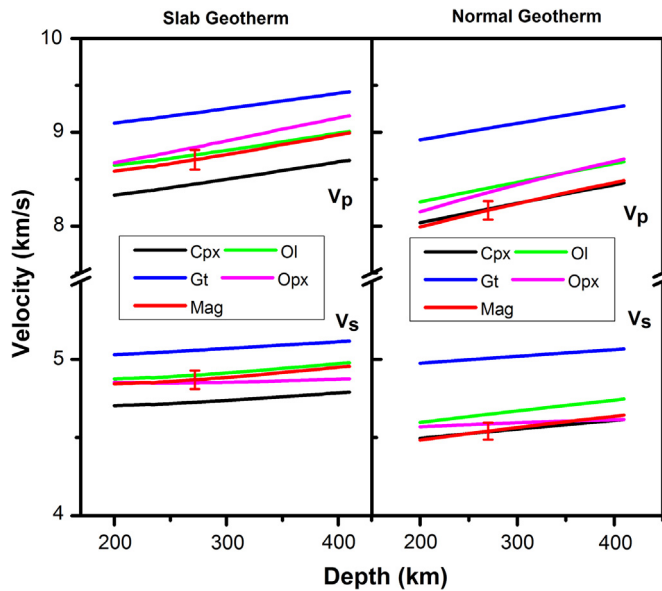


**Fig. 8.** Modeled velocities of the major constituent minerals in peridotite and eclogite along an expected normal-mantle geotherm (Dziewonski and Anderson, 1981; Brown and Shankland, 1981) and an expected subducting-slab geotherm (Peacock, 2003). Red lines: magnesite (Mag) (this study); blue lines: garnet (Gt) (Thieblot et al., 1998; Lu et al., 2013); green lines: olivine (Ol) (Isaak, 1992; Zha et al., 1998; Liu and Li, 2006); magenta lines: Orthopyroxene (Opx) (Chai et al., 1997; Jackson et al., 2003, 2007); black lines: clinopyroxene (Cpx) (Cameron, 1973; Finger and Ohashi, 1976; Duffy and Anderson, 1989; Collins and Brown, 1998). (For interpretation of the references to color in this figure legend, the reader is referred to the web version of this article.)

from 200-km to 410-km depth, because the mineralogical, geochemical, and seismic heterogeneities above 200 km depth are much more complex (Jordan, 1975; Grand and Helmberger, 1984; Hofmann, 2003). Specifically, the existence of the low-velocity zone at approximately 200 km depth would require further considerations of a partially-melted mantle model (Zhao et al., 1992; Webb and Forsyth, 1998).

Our modeled velocities show that magnesite and clinopyroxene have the lowest  $V_p$  and  $V_s$  among all mantle minerals along a normal geotherm, while garnet has the highest velocity. Along a cold slab geotherm, however, the  $V_p$  and  $V_s$  velocities of magnesite are closer to that of olivine, rather than that of clinopyroxene with the lowest velocity profiles. This difference can be understood in terms of the sensitivity of the elastic moduli of magnesite to change in temperature that is larger than that of the aforementioned major mantle minerals. The  $dK/dT$  and  $dG/dT$  of magnesite are  $-0.024$  ( $\pm 0.002$ ) GPa/K and  $-0.0148$  ( $\pm 0.0007$ ) GPa/K, respectively, while clinopyroxene has  $dK/dT = -0.013$  GPa/K and  $dG/dT = -0.01$  GPa/K (Duffy and Anderson, 1989). Considering the average Fe/Mg molar ratio of approximately 0.12 in the Earth's mantle (McDonough and Sun, 1995), magnesite is expected to contain approximately 15 wt.% iron in the upper mantle (e.g. Dasgupta et al., 2004). The addition of 15 wt.% iron in magnesite is expected to decrease the velocity profiles by 3–4% at ambient condition (Sanchez-Valle et al., 2011), although the effect of iron on the elasticity of magnesite at high  $P-T$  conditions remains to be further investigated (Lin et al., 2012).

#### 4.2. Velocity profiles of the carbon-bearing eclogite and peridotite

To further evaluate the effect of carbonate presence on the seismic velocity profiles of the Earth's upper mantle and to place constraints on the seismic detectability of the deep-mantle carbonate, we have also calculated the velocity profiles of eclogite and peridotite containing 5 wt.%  $\text{CO}_2$  in the form of magnesite

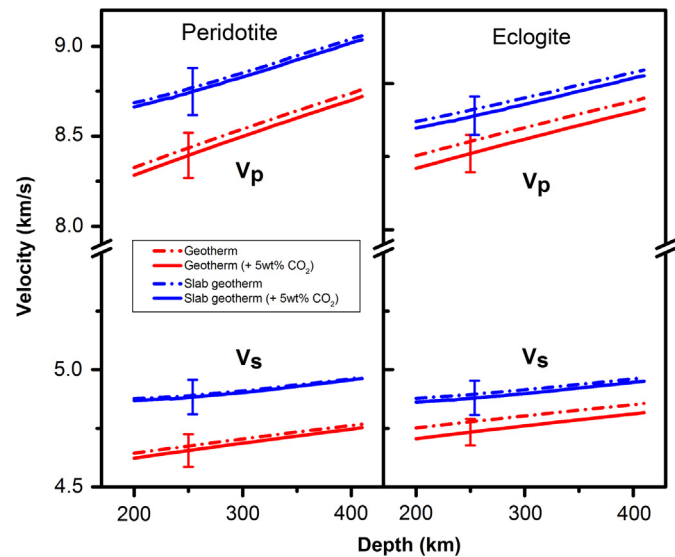


**Fig. 9.** Modeled velocity profiles of carbon-free and carbon-bearing peridotite and eclogite along an expected normal-mantle geotherm in the upper mantle (Dziewonski and Anderson, 1981; Brown and Shankland, 1981). Mineralogical compositions and proportions are: for carbon-free eclogite: 53.3 wt.% garnet and 46.7 wt.% clinopyroxene; for carbon-free peridotite: 59.3 wt.% olivine, 12.8 wt.% clinopyroxene, 11.4 wt.% orthopyroxene, 16.5 wt.% garnet. 5 wt.%  $\text{CO}_2$  (10 wt.%  $\text{MgCO}_3$  in eclogite and 10 wt.% in peridotite) content in the form of magnesite was used in the compositional model for the carbon-bearing eclogite and peridotite (Dasgupta et al., 2004; Dasgupta and Hirschmann, 2006).

(Fig. 9). Here we have used the mineral proportions reported for carbonated eclogite (Dasgupta et al., 2004) and peridotite (Dasgupta and Hirschmann, 2006) as representative references for comparisons of the velocity profiles. The mineral assemblage in carbon-free eclogite model includes approximately 53.3 wt.% garnet and 46.7 wt.% clinopyroxene, while carbon-free peridotite includes 59.3 wt.% olivine, 12.8 wt.% clinopyroxene, 11.4 wt.% orthopyroxene, and 16.5 wt.% garnet. 5 wt.%  $\text{CO}_2$  (10 wt.%  $\text{MgCO}_3$  in eclogite and 10 wt.% in peridotite) content in the form of magnesite was used in the compositional modeling as a carbonated eclogite and peridotite in order to better understand the sensitivity of the carbonation effects, although these rock assemblages are expected to contain much less  $\text{CO}_2$  (Dasgupta and Hirschmann, 2010). Our modeled results along a normally expected geotherm (Dziewonski and Anderson, 1981; Brown and Shankland, 1981) show that addition of 5 wt.%  $\text{CO}_2$  decreases the  $V_p$  and  $V_s$  by less than 1%, while the change is less than 0.5% along an expected geotherm for a cold subducted slab (Peacock, 2003) (Fig. 9). We note that standard propagations of the errors involved in these calculations show that the standard deviation ( $\pm \sigma$ ) in the  $V_p$  and  $V_s$  values is approximately 2% (Fig. 9), meaning that these changes in the  $V_p$  and  $V_s$  profiles are all within the uncertainty and can be considered as negligible from a mineral physics prospective.

#### 4.3. $V_p$ and $V_s$ anisotropy of magnesite at relevant $P-T$ conditions of the upper mantle

Using the modeled elastic constants of magnesite at expected  $P-T$  conditions of the upper mantle, the azimuthal  $V_p$  anisotropy and shear-wave splitting of magnesite are calculated along a normal geotherm (Fig. S1).  $V_p$  and  $V_s$  anisotropies of other major minerals expected to be present in the peridotite and eclogite assemblages are also calculated for comparison including olivine (Isaak, 1992; Abramson et al., 1997; Zha et al., 1998; Liu and Li, 2006), orthopyroxene (Chai et al., 1997; Jackson et al., 2003, 2007), clinopyroxene (Finger and Ohashi, 1976; Matsui and Busing, 1984; Isaak et al., 2006), and garnet (Thieblot et al., 1998; Lu et al., 2013).

Magnesite exhibits approximately 37–41% azimuthal  $V_P$  anisotropy and 45–49% shear wave splitting anisotropy at expected  $P-T$  conditions of the upper mantle. These results show that magnesite exhibits much larger  $V_P$  and  $V_S$  anisotropies than other major mantle minerals and that these anisotropies increase with increasing depth.

## 5. Deep-Earth implications and conclusions

Recent geophysical and geochemical studies have shown that peridotite and eclogite are the most likely rock assemblages in deeper upper mantle and subduction zones (Nicolas and Christensen, 1987; Johnson et al., 1990; Spandler et al., 2003), respectively, in which they may contain amounts of  $\text{CO}_2$  in the form of accessory iron-bearing magnesite, ferromagnesite, with approximately 15 wt.% iron (e.g. Dasgupta et al., 2004). Ferromagnesite can be transported into these regions through the subduction of carbonate minerals in subducted slabs, and remains stable as a major deep-carbon host (Luth, 1999). Our modeled velocity profiles of magnesite at relevant  $P-T$  conditions of the upper mantle indicate that the existence of 5 wt.%  $\text{CO}_2$  in the form of magnesite only produces less than 1% reductions in  $V_P$  and  $V_S$  velocities as compared to the carbon-free counterparts. Considering the uncertainties in our results as well as seismic models, we thus conclude that seismic observations of the moderately carbonated regions that are of relevant geochemical abundances in the upper mantle will be challenging.

An electronic high-spin to low-spin transition of iron has been recently reported to occur in ferromagnesite ( $\text{Mg}_{0.35}\text{Fe}_{0.65}\text{CO}_3$ ) at approximately 45 GPa ( $\sim 1000$  km in depth) (Lin et al., 2012, 2013). The transition of iron in ferromagnesite from the high-spin to the low-spin state results in a density increase by approximately 6% and an incompressibility increase by 8% (Lavina et al., 2009, 2010; Lin et al., 2012, 2013), indicating that low-spin ferromagnesite can become relatively denser than the high-spin counterpart below the middle part of the lower mantle. Changes in the sound velocities within the spin transition of iron in the lower-mantle ferropericlase have also been reported recently (e.g. Lin et al., 2013; Marquardt et al., 2009; Wu et al., 2013). It is thus conceivable that the spin transition can also affect the sound velocities of ferromagnesite, influencing the modeled seismic profiles presented here.

Our modeled results for elastic anisotropies show that magnesite exhibits approximately 37–41%  $V_P$  anisotropy and 46–49%  $V_S$  splitting anisotropy at upper-mantle  $P-T$  conditions, making it the highest anisotropic mineral when compared with other major mantle minerals (Fig. S1). Furthermore, the anisotropies of magnesite increase with increasing  $P-T$  (depth) that is in contrast to most other major upper-mantle minerals. Given the fact that carbonates (e.g. calcite, magnesite, dolomite) are markedly weaker in creep strength than other major minerals in peridotite and eclogite assemblages (Schneider, 1976; Karato, 1989) and that they tend to develop fabrics under deviatoric stress or plastic flow conditions (Schmid et al., 1987; Rutter et al., 1994), it is thus possible that seismic velocity anisotropies can be used as a diagnostic feature for detections of the highly carbonated materials containing textured magnesite in the Earth's mantle. Recent studies have indeed demonstrated that carbonation of peridotite may produce high seismic anisotropy due to the high elastic anisotropy of carbonate minerals (Brownlee et al., 2013). Recent results on the lattice preferred orientation (LPO) or fabrics have shown that calcite can develop a moderately strong crystallographic preferred orientation with the  $c$ -axes sub-perpendicular to a foliation developed during localized high-pressure deformations (Brady et al., 2004), which can be used as an analog to understand the deformation of magnesite in the mantle. If magnesite develops similar fabrics in the carbonated peridotite and eclogite, its minimum  $P$ -wave velocity

would likely be normal to the foliation while the maximum shear wave splitting will be sub-parallel to the foliation. Future studies on the deformation mechanism of magnesite in the carbonated eclogite and peridotite at relevant  $P-T$  condition are needed to shed new light on the role of the magnesite carbonate on seismic anisotropies of the Earth's upper mantle.

## Acknowledgements

J.F. Lin acknowledges supports from the Sloan Foundation's Deep Carbon Observatory, the US National Science Foundation (EAR-1053446 and EAR-1056670), and the Carnegie/DOE Alliance Center (CDAC). Synchrotron works of the study were performed at GSECARS of the APS, ANL. APS is supported by DOE-BES, under Contract No. DE-AC02-06CH11357. GeoSoilEnviroCARS is supported by the National Science Foundation – Earth Sciences, Department of Energy and the State of Illinois. The authors also thank K. Zhuravlev for technical assistance and C. Lu and D. Fan for constructive discussions and L. Dafoe for editing the manuscript.

## Appendix A. Supplementary material

Supplementary material related to this article can be found online at <http://dx.doi.org/10.1016/j.epsl.2014.01.027>.

## References

- Abramson, E., Brown, J., Slutsky, L., Zaug, J., 1997. The elastic constants of San Carlos olivine to 17 GPa. *J. Geophys. Res.* 102, 12253–12263.
- Birch, F., 1978. Finite strain isotherm and velocities for single-crystal and polycrystalline NaCl at high pressures and 300 K. *J. Geophys. Res.* 83, 1257–1268.
- Boulard, E., Gloter, A., Corgne, A., Antonangeli, D., Auzende, A.L., Perrillat, J.P., Guyot, F., Fiquet, G., 2011. New host for carbon in the deep Earth. *Proc. Natl. Acad. Sci. USA* 108, 5184–5187.
- Brady, J.B., Markley, M.J., Schumacher, J.C., Cheney, J.T., Bianciardi, G.A., 2004. Aragonite pseudomorphs in high-pressure marbles of Syros, Greece. *J. Struct. Geol.* 26, 3–9.
- Brenker, F.E., Vollmer, C., Vincze, L., Vekemans, B., Szymanski, A., Janssens, K., Szabolcsi, I., Nasdala, L., Joswig, W., Kaminsky, F., 2007. Carbonates from the lower part of transition zone or even the lower mantle. *Earth Planet. Sci. Lett.* 260, 1–9.
- Brey, G., Brice, W.R., Ellis, D.J., Green, D.H., Harris, K.L., Ryabchikov, I.D., 1983. Pyroxene–carbonate reactions in the upper mantle. *Earth Planet. Sci. Lett.* 62, 63–74.
- Brey, G.P., Bulatov, V.K., Girnis, A.V., Lahaye, Y., 2008. Experimental melting of carbonated peridotite at 6–10 GPa. *J. Petrol.* 49, 797–821.
- Brown, J., Shankland, T., 1981. Thermodynamic parameters in the Earth as determined from seismic profiles. *Geophys. J. R. Astron. Soc.* 66, 579–596.
- Brownlee, S.J., Hacker, B.R., Harlow, G.E., Seward, G., 2013. Seismic signatures of a hydrated mantle wedge from antigorite crystal-preferred orientation (CPO). *Earth Planet. Sci. Lett.* 375, 395–407.
- Burton, M.R., Sawyer, G.M., Granieri, D., 2013. Deep carbon emissions from volcanoes. *Rev. Mineral. Geochim.* 75, 323–354.
- Cameron, M., 1973. High-temperature crystal chemistry of acmite, diopside, hedenbergite, jadeite, spoumene, and ureyite. *Am. Mineral.* 58, 594–618.
- Chai, M., Brown, J.M., Slutsky, L.J., 1997. The elastic constants of an aluminous orthopyroxene to 12.5 GPa. *J. Geophys. Res.* 102, 14779–14785.
- Chen, C.C., Lin, C.C., Liu, L.G., Sinogeikin, S.V., Bass, J.D., 2001. Elasticity of single-crystal calcite and rhodochrosite by Brillouin spectroscopy. *Am. Mineral.* 86, 1525–1529.
- Chen, P.F., Chiao, L.Y., Huang, P., Yang, Y., Liu, L., 2006. Elasticity of magnesite and dolomite from a genetic algorithm for inverting Brillouin spectroscopy measurements. *Phys. Earth Planet. Inter.* 155, 73–86.
- Christensen, N.I., 1972. Elastic properties of polycrystalline magnesium, iron, and manganese carbonates to 10 kilobars. *J. Geophys. Res.* 77, 369–372.
- Collins, M., Brown, J., 1998. Elasticity of an upper mantle clinopyroxene. *Phys. Chem. Miner.* 26, 7–13.
- Dasgupta, R., Hirschmann, M.M., 2006. Melting in the Earth's deep upper mantle caused by carbon dioxide. *Nature* 440, 659–662.
- Dasgupta, R., Hirschmann, M.M., 2010. The deep carbon cycle and melting in Earth's interior. *Earth Planet. Sci. Lett.* 298, 1–13.
- Dasgupta, R., Hirschmann, M.M., Withers, A.C., 2004. Deep global cycling of carbon constrained by the solidus of anhydrous, carbonated eclogite under upper mantle conditions. *Earth Planet. Sci. Lett.* 227, 73–85.

- Duffy, T.S., Anderson, D.L., 1989. Seismic velocities in mantle minerals and the mineralogy of the upper mantle. *J. Geophys. Res., Solid Earth* 94, 1895–1912.
- Dziewonski, A.M., Anderson, D.L., 1981. Preliminary reference Earth model. *Phys. Earth Planet. Inter.* 25, 297–356.
- Every, A., 1980. General closed-form expressions for acoustic waves in elastically anisotropic solids. *Phys. Rev. B* 22, 1746–1760.
- Finger, L., Ohashi, Y., 1976. The thermal expansion of diopside to 800 °C and a refinement of the crystal structure at 700 °C. *Am. Mineral.* 61, 303–310.
- Grand, S.P., Helmberger, D.V., 1984. Upper mantle shear structure of North America. *Geophys. J. R. Astron. Soc.* 76, 399–438.
- Hazen, R.M., Hemley, R.J., Mangum, A.J., 2012. Carbon in Earth's interior: Storage, cycling, and life. *Eos* 93, 17–18.
- Hearmon, R., 1984. The Elastic Constants of Crystals and Other Anisotropic Materials. Landolt-Börnstein: Numerical Data and Functional Relationships in Science and Technology, vol. 11.
- Hill, R., 1952. The elastic behaviour of a crystalline aggregate. *Proc. Phys. Soc. A* 65, 349–354.
- Hirschmann, M.M., Dasgupta, R., 2009. The H/C ratios of Earth's near-surface and deep reservoirs, and consequences for deep Earth volatile cycles. *Chem. Geol.* 262, 4–16.
- Hofmann, A., 2003. Sampling mantle heterogeneity through oceanic basalts: isotopes and trace elements. In: *Treatise on Geochemistry*, vol. 2, pp. 61–101.
- Hubert, P., Plicque, F., 1972. Propriétés élastiques de carbonates rhomboédriques monocristallins: Calcite, magnésite, dolomite. *C. R. Acad. Sci. Paris* 275, 391–394.
- Isaak, D.G., 1992. High-temperature elasticity of iron-bearing olivines. *J. Geophys. Res., Solid Earth* 97, 1871–1885.
- Isaak, D., Ohno, I., Lee, P., 2006. The elastic constants of monoclinic single-crystal chrome-diopside to 1300 K. *Phys. Chem. Miner.* 32, 691–699.
- Isshiki, M., Irfune, T., Hirose, K., Ono, S., Ohishi, Y., Watanuki, T., Nishibori, E., Takata, M., Sakata, M., 2004. Stability of magnesite and its high-pressure form in the lowermost mantle. *Nature* 427, 60–63.
- Jackson, J.M., Palko, J.W., Andrault, D., Sinogeikin, S.V., Lakshtanov, D.L., Jingyun, W., Chang-Sheng, Z., 2003. Thermal expansion of natural orthoenstatite to 1473 K. *Eur. J. Mineral.* 15, 469–473.
- Jackson, J.M., Sinogeikin, S.V., Bass, J.D., 2007. Sound velocities and single-crystal elasticity of orthoenstatite to 1073 K at ambient pressure. *Phys. Earth Planet. Inter.* 161, 1–12.
- Johnson, K., Dick, H.J., Shimizu, N., 1990. Melting in the oceanic upper mantle: an ion microprobe study of diopsides in abyssal peridotites. *J. Geophys. Res., Solid Earth* 95, 2661–2678.
- Jordan, T.H., 1975. Lateral heterogeneity and mantle dynamics. *Nature* 257, 745–750.
- Kaminsky, F.V., Wirth, R., 2011. Iron carbide inclusions in lower-mantle diamond from Juina, Brazil. *Can. Mineral.* 49, 555–572.
- Kantor, I., Prakapenka, V., Kantor, A., Dera, P., Kurnosov, A., Sinogeikin, S., Dubrovinskaia, N., Dubrovinsky, L., 2012. BX90: A new diamond anvil cell design for X-ray diffraction and optical measurements. *Rev. Sci. Instrum.* 83, 125102–125106.
- Karato, S.-i., 1989. Plasticity-crystal structure systematics in dense oxides and its implications for the creep strength of the Earth's deep interior: a preliminary result. *Phys. Earth Planet. Inter.* 55, 234–240.
- Lavina, B., Dera, P., Downs, R., Prakapenka, V., Rivers, M., Sutton, S., Nicol, M., 2009. Siderite at lower mantle conditions and the effects of the pressure-induced spin-pairing transition. *Geophys. Res. Lett.* 36, L23306.
- Lavina, B., Dera, P., Downs, R.T., Tschauner, O., Yang, W., Shebanova, O., Shen, G., 2010. Effect of dilution on the spin pairing transition in rhombohedral carbonates. *High Press. Res.* 30, 224–229.
- Lin, J.F., Liu, J., Jacobs, C., Prakapenka, V.B., 2012. Vibrational and elastic properties of ferromagnesite across the electronic spin-pairing transition of iron. *Am. Mineral.* 97, 583–591.
- Lin, J.F., Speziale, S., Mao, Z., Marquardt, H., 2013. Effects of the electronic spin transitions of iron in lower mantle minerals: Implications for deep mantle geo-physics and geochemistry. *Rev. Geophys.* 51, 244–275.
- Litasov, K.D., Fei, Y., Ohtani, E., Kurabayashi, T., Funakoshi, K., 2008. Thermal equation of state of magnesite to 32 GPa and 2073 K. *Phys. Earth Planet. Inter.* 168, 191–203.
- Liu, W., Li, B., 2006. Thermal equation of state of  $(\text{Mg}_{0.9}\text{Fe}_{0.1})_2\text{SiO}_4$  olivine. *Phys. Earth Planet. Inter.* 157, 188–195.
- Lu, C., Mao, Z., Lin, J.F., Zhuravlev, K.K., Tkachev, S.N., Prakapenka, V.B., 2013. Elasticity of single-crystal iron-bearing pyrope up to 20 GPa and 750 K. *Earth Planet. Sci. Lett.* 361, 134–142.
- Luth, R.W., 1999. Carbon and carbonates in the mantle. In: *Mantle Petrology: Field Observations and High Pressure Experimentation: a Tribute to Francis R. (Joe) Boyd*. In: *Geochem. Soc. Spec. Publ.*, vol. 6, pp. 297–316.
- Mainprice, D., 1990. A FORTRAN program to calculate seismic anisotropy from the lattice preferred orientation of minerals. *Comput. Geosci.* 16, 385–393.
- Mainprice, D., Barruol, G., Ismail, W.B., 2000. The seismic anisotropy of the Earth's mantle: from single crystal to polycrystal. In: *Geophys. Monogr.*, vol. 117. American Geophysical Union, pp. 237–264.
- Mao, H.K., Xu, J., Bell, P.M., 1986. Calibration of the ruby pressure gauge to 800 kbar under quasi-hydrostatic conditions. *J. Geophys. Res.* 91, 4673–4676.
- Mao, Z., Armentrout, M., Rainey, E., Manning, C.E., Dera, P., Prakapenka, V.B., Kavner, A., 2011. Dolomite III: A new candidate lower mantle carbonate. *Geophys. Res. Lett.* 38, L22303.
- Mao, Z., Lin, J.F., Jacobsen, S.D., Duffy, T.S., Chang, Y.Y., Smyth, J.R., Frost, D.J., Hauri, E.H., Prakapenka, V.B., 2012. Sound velocities of hydrous ringwoodite to 16 GPa and 673 K. *Earth Planet. Sci. Lett.* 331, 112–119.
- Marquardt, H., Speziale, S., Reichmann, H.J., Frost, D.J., Schilling, F.R., Garnero, E.J., 2009. Elastic shear anisotropy of ferropericlase in Earth's lower mantle. *Science* 324, 224.
- Matsui, M., Busing, W.R., 1984. Calculation of the elastic constants and high-pressure properties of diopside,  $\text{CaMgSi}_2\text{O}_6$ . *Am. Mineral.* 69, 1090–1095.
- McDonough, W.F., Sun, S.S., 1995. The composition of the Earth. *Chem. Geol.* 120, 223–253.
- Molina, J.F., Poli, S., 2000. Carbonate stability and fluid composition in subducted oceanic crust: an experimental study on  $\text{H}_2\text{O}-\text{CO}_2$  bearing basalts. *Earth Planet. Sci. Lett.* 176, 295–310.
- Nelson, D.F., Lazay, P.D., Lax, M., 1972. Brillouin scattering in anisotropic media: calcite. *Phys. Rev. B* 6, 3109–3120.
- Nicolas, A., Christensen, N.I., 1987. Formation of anisotropy in upper mantle peridotites—a review. In: *Composition, Structure and Dynamics of the Lithosphere–Asthenosphere System*, pp. 111–123.
- Oganov, A.R., Glass, C.W., Ono, S., 2006. High-pressure phases of  $\text{CaCO}_3$ : Crystal structure prediction and experiment. *Earth Planet. Sci. Lett.* 241, 95–103.
- Oganov, A.R., Ono, S., Ma, Y., Glass, C.W., Garcia, A., 2008. Novel high-pressure structures of  $\text{MgCO}_3$ ,  $\text{CaCO}_3$  and  $\text{CO}_2$  and their role in Earth's lower mantle. *Earth Planet. Sci. Lett.* 273, 38–47.
- Ostwald, J., Pazold, W., Weis, O., 1977. High-resolution Brillouin spectroscopy of water. *Appl. Phys.* 13, 351–356.
- Peacock, S.M., 2003. Thermal structure and metamorphic evolution of subducting slabs. In: *Geophys. Monogr.*, vol. 138. American Geophysical Union, pp. 7–22.
- Poirier, J.P., 2000. Introduction to the Physics of the Earth's Interior. Cambridge University Press.
- Polian, A., Vo-Thanh, D., Richet, P., 2002. Elastic properties of  $\alpha\text{-SiO}_2$  up to 2300 K from Brillouin scattering measurements. *Europ. Phys. Lett.* 57, 375.
- Ross, N.L., 1997. The equation of state and high-pressure behavior of magnesite. *Am. Mineral.* 82, 682–688.
- Rutter, E., Casey, M., Burlini, L., 1994. Preferred crystallographic orientation development during the plastic and superplastic flow of calcite rocks. *J. Struct. Geol.* 16, 1431–1446.
- Sanchez-Valle, C., Ghosh, S., Rosa, A.D., 2011. Sound velocities of ferromagnesian carbonates and the seismic detection of carbonates in eclogites and the mantle. *Geophys. Res. Lett.* 38, L24315.
- Schmid, S., Panozzo, R., Bauer, S., 1987. Simple shear experiments on calcite rocks: rheology and microfabric. *J. Struct. Geol.* 9, 747–778.
- Schneider, H., 1976. The progressive crystallization and ordering of low-temperature dolomites. *Mineral. Mag.* 40, 579–587.
- Scott, H.P., Doczy, V.M., Frank, M.R., Hasan, M., Lin, J.-F., Yang, J., 2013. Magnesite formation from  $\text{MgO}$  and  $\text{CO}_2$  at the pressures and temperatures of Earth's mantle. *Am. Mineral.* 98, 1211–1218.
- Sinogeikin, S.V., Bass, J.D., 2000. Single-crystal elasticity of pyrope and  $\text{MgO}$  to 20 GPa by Brillouin scattering in the diamond cell. *Phys. Earth Planet. Inter.* 120, 43–62.
- Sinogeikin, S., Bass, J., Prakapenka, V., Lakshtanov, D., Shen, G., Sanchez-Valle, C., Rivers, M., 2006. Brillouin spectrometer interfaced with synchrotron radiation for simultaneous x-ray density and acoustic velocity measurements. *Rev. Sci. Instrum.* 77, 103905.
- Spandler, C., Hermann, J., Arculus, R., Mavrogenes, J., 2003. Redistribution of trace elements during prograde metamorphism from lawsonite blueschist to eclogite facies: implications for deep subduction-zone processes. *Contrib. Mineral. Petro.* 146, 205–222.
- Stixrude, L., Lithgow-Bertelloni, C., 2005. Thermodynamics of mantle minerals—I. Physical properties. *Geophys. J. Int.* 162, 610–632.
- Thieblot, L., Roux, J., Richet, P., 1998. High-temperature thermal expansion and decomposition of garnets. *Eur. J. Mineral.* 10, 7–15.
- Webb, S.C., Forsyth, D.W., 1998. Structure of the upper mantle under the EPR from waveform inversion of regional events. *Science* 280, 1227–1229.
- Wu, J., Buseck, P.R., 2013. Carbon storage at defect sites in mantle mineral analogues. *Nat. Geosci.* 6, 875–878.
- Wu, Z., Justo, J.F., Wentzcovitch, R.M., 2013. Elastic anomalies in a spin-crossover system: ferropericlase at lower mantle conditions. *Phys. Rev. Lett.* 110, 228501.
- Yaxley, G.M., Green, D.H., 1994. Experimental demonstration of refractory carbonate-bearing eclogite and siliceous melt in the subduction regime. *Earth Planet. Sci. Lett.* 128, 313–325.
- Zha, C., Duffy, T.S., Downs, R.T., Mao, H., Hemley, R.J., 1998. Brillouin scattering and X-ray diffraction of San Carlos olivine: direct pressure determination to 32 GPa. *Earth Planet. Sci. Lett.* 159, 25–33.
- Zhao, D., Hasegawa, A., Horiuchi, S., 1992. Tomographic imaging of P and S wave velocity structure beneath northeastern Japan. *J. Geophys. Res.* 97, 19909–19928.